Chinese Chemical Letters 32 (2021) 1181–1185

Contents lists available at ScienceDirect

Chinese Chemical Letters

journal homepage: www.elsevier.com/locate/cclet

Communication

Porous microtubes of nickel-cobalt double oxides as non-enzymatic hydrogen peroxide sensors

Qin Li[a,b], Jin Niu[a,b], Meiling Dou[a,b], Zhengping Zhang[a,b,*], Feng Wang[a,b,*]

[a] State Key Laboratory of Chemical Resource Engineering, Beijing Key Laboratory of Electrochemical Process and Technology for Materials, Beijing University of Chemical Technology, Beijing 100029, China
[b] Beijing Advanced Innovation Center for Soft Matter Science and Engineering, Beijing University of Chemical Technology, Beijing 100029, China

ARTICLE INFO

Article history:
Received 15 May 2020
Received in revised form 10 June 2020
Accepted 26 July 2020
Available online 29 July 2020

Keywords:
Double metal oxides
Porous microtubes
Oxygen vacancies
Hydrogen peroxide detection
Electrochemical sensors

ABSTRACT

Non-enzymatic electrochemical sensors for the determination of hydrogen peroxide (H_2O_2) have attracted more and more concerns. A series of nickel and cobalt double oxides (Ni_xCo_y-DO) with the different ratios of Ni/Co have been prepared by a polyol-mediated solvothermal method for H_2O_2 detection. The obtained products exhibit honeycomb-like open porous microtubes constituted with the low-dimensional nanostructured Ni_xCo_y-DO blocks after the calcination treatment. Compared with nickel oxides, the introduced Co ions in Ni_xCo_y-DO can induce the production of surficial oxygen vacancies, and further enhance the electrode surface activity. In particular, the NiCo-DO sample (with an atomic ratio of Ni/Co = 4:3) shows the richest surficial oxygen vacancies and presents the highest H_2O_2 detection activity among all the as-prepared samples, demonstrating an excellent sensitivity of 698.60 μA L $mmol^{-1}$ cm^{-2} (0 ~ 0.4 mmol/L), low detection limit (0.28 μmol/L, S/N = 3), as well as long stability, high selectivity and good reproducibility. This work lends a new impetus to the potential application of double metal oxides for the next generation of non-enzymatic sensors.

Hydrogen peroxide (H_2O_2), as a strong oxidizing agent, not only plays an important role in pharmaceutics, industrial bleaches and clinical medicine [1–3], but also can induce many diseases, such as cardiovascular disease, Alzheimer's, cancer, Parkinson's disease [4,5]. Therefore, it is essential to accurately detect the concentration of H_2O_2 with a simple and cost-effective operation method. Among various detection approaches [6–8], non-enzymatic electrochemical sensors have attracted more and more attention due to their irreplaceable advantages, including low detection limit, high sensitivity, good selectivity and high stability [9,10]. Accordingly, a wide variety of non-enzymatic sensor materials have been investigated, such as precious metals (Ag, Au, *etc.*) [11,12], carbon materials [13], and non-precious metal compounds [14–16]. Due to the balance of availability and detection performance, nickel oxides (NiO) have been considered as one of the efficient H_2O_2 sensing materials [17,18]. The detection mechanism is based on the increased anodic current responses of Ni(II)O → Ni(III)OOH, attributed to the electron transfer from H_2O_2 to Ni(III)OOH, according to Eqs. 1 and 2 [19].

$$Ni(II)O + OH^- \leftrightarrow Ni(III)OOH + e^- \quad (1)$$

$$2Ni(III)OOH + H_2O_2 \rightarrow 2Ni(II)O + 2H_2O + O_2 \quad (2)$$

Nevertheless, the utilization of NiO particles directly as the electrochemical sensors is limited by their high electronic resistance, confined surface area and inferior surficial activity. Hence, several featured NiO nanoarchitectures (*e.g.*, nanoparticles [20], nanofibers [21], nanosheets [22], nanoflower [23], *etc.*) have been designed to enlarge the electrochemical surface area. In particular, the low-dimensional crosslinked texture with open pores has proved to be favorable for enhancing electronic conductivity and facilitating mass-transfer ability. Besides optimizing nanostructures, introducing other metals into NiO has been investigated to enhance the reactivity by the complementary and synergistic effects of the two types of metal elements [24,25]. Among these metal elements, Co has the similar atomic radius to Ni, which is beneficial for incorporating Co into NiO lattice to form well-dispersion Ni–O–Co solid solutions for enhancing the electrochemical reactivity [26]. To this end, it is necessary to systematically investigate the role of Ni and Co, but such research has been rarely reported, especially for H_2O_2 detection.

* Corresponding authors at: State Key Laboratory of Chemical Resource Engineering, Beijing Key Laboratory of Electrochemical Process and Technology for Materials, Beijing University of Chemical Technology, Beijing 100029, China.
E-mail addresses: zhangzhengping@mail.buct.edu.cn (Z. Zhang), wangf@mail.buct.edu.cn (F. Wang).

https://doi.org/10.1016/j.cclet.2020.07.045
1001-8417/

In this work, we synthesized a series of honeycomb-like open porous nanoarchitecture built of the low-dimensional nickel and cobalt double oxides (Ni_xCo_y-DO) blocks for H_2O_2 detection (Supporting information). After two simple synthesis steps, involving of polyol-mediated solvothermal reaction and calcination (Scheme S1 in Supporting information), different contents of Co were successfully incorporated into NiO. The obtained samples were named as Ni_2Co-DO, NiCo-DO and $NiCo_2$-DO, respectively, according to the mass ratios of metal precursors (*i.e.*, Ni/Co chlorides added was 2:1, 1:1, and 1:2). The Ni/Co atomic ratios were measured as 5:2 (Ni_2Co-DO), 4:3 (NiCo-DO) and 2:3 ($NiCo_2$-DO) by inductively coupled plasma (ICP, Table S1 in Supporting information). In comparison with the homemade NiO, the introduced Co ions in Ni_xCo_y-DO not only facilitated the construction of honeycomb-like open porous microtubes but also induced the production of surficial oxygen vacancies. As a result, the Ni_xCo_y-DO exhibited high detection performance as non-enzymatic H_2O_2 electrochemical sensors.

The Ni_xCo_y layered double hydroxide (Ni_xCo_y-LDH) and Ni hydroxide intermediates were firstly characterized by X-ray powder diffraction (XRD) and scanning electron microscopy (SEM). From XRD patterns (Fig. S1 in Supporting information), the characteristic diffraction peaks centered at 10.3°, 21.6°, 33.8°, 60.1° refers to the (003), (006), (101), (110) crystal planes of α-Co/$Ni(OH)_2$ [27], suggesting that all the hydroxide intermediates were generated. On the contrary, no solid product was obtained by the same synthetic method in the absence of Ni ions (Fig. S2 in Supporting information). As shown in SEM in Fig. S3 (Supporting information), compared with the uniform microspheres of $Ni(OH)_2$ intermediate (d = 850 nm), Ni_xCo_y-LDH presented that the microspheres were assembled in one-dimension structure with the increase of Co content. Since the mass ratio of Ni/Co chlorides added to the system was below 1:1, the microspheres almost disappeared and formed open porous microtubules structure (d = 2.6 μm) constituted with a great number of crosslinked and vertically-standing nanoflakes. The morphologic variety of $Ni(OH)_2$ and Ni_xCo_y-LDH originated from a larger solubility product of Co^{2+} than Ni^{2+} [28], resulting to that the Co^{2+} ions served as "glue" to reconstitute the microtubules with the $Ni(OH)_2$ microspheres [29,30]. After the calcination treatment, all the final products (*i.e.*, Ni_xCo_y-DO and NiO) still reserved the porous microarchitecture of the hydroxide intermediates with a slight reduction in diameter (Ni_xCo_y-DO: d = 2.1 μm; NiO: d = 770 nm, Figs. 1a–d). Meanwhile, the internal structures of these microtubules were clearly discerned by the high-resolution transmission electron microscopy (HR-TEM). As shown in Fig. 1e, the NiO was composed of nanoscale but irregular features, and had an interplanar spacing about 0.24 nm, which could be corresponded to the NiO (111) plane. Compared with the NiO, the lattice fringes with 0.24 nm of Ni_xCo_y-DO were rougher, indicating that lattice defects increased after Co introducing (Figs. 1f–h) [31]. In addition, it could be seen that the formation of nanorod was promoted by increasing the Co content in Ni_xCo_y-DO (Fig. S4 in Supporting information), and the nanorods resolved lattice fringes with an interplanar spacing of about 0.47 nm. Furthermore, the elemental mapping images of NiCo-DO sample (Fig. S5 in Supporting information) demonstrated that the element Ni, Co and O were evenly distributed in the microtubules. On the basis of the microscopy observation, the illustrations of morphology variety for NiO and Ni_xCo_y-DO are summarized in Fig. 1i.

To investigate the porous structure of these as-prepared samples, N_2 adsorption-desorption measurements were conducted for NiO, Ni_2Co-DO, NiCo-DO and $NiCo_2$-DO (Fig. S6 and Table S2 in Supporting information). With the increase of Co content, the Ni_xCo_y-DO samples presented the decreased surface area (from 102.9 m^2/g to 86.9 m^2/g), but increased pore volume (from 0.166 cm^3/g to 0.223 cm^3/g) and average pore size (from 7.5 nm to 12.2 nm). Owing to the large divergence in the morphologies between Ni_xCo_y-DO and NiO samples, the porous parameters of NiO (93.5 m^2/g, 0.231 cm^3/g and 8.3 nm) did not follow this tendency. The larger surface area of Ni_xCo_y-DO, than those of previously reported Ni-Co oxides [32,33], could be attributed to the polyol-mediated effect, especially polyethylene glycol [34].

Fig. 2a showed the XRD patterns of Ni_xCo_y-DO and NiO samples, and the characteristic diffraction peaks of NiO sample were assigned to the fine cubic rock salt structure (JCPDS No. 47-1049). When the Co content was increased, the diffraction peaks of Ni_2Co-DO and NiCo-DO became weaker and broader, but mainly maintained the NiO-based crystal structure. However, as for $NiCo_2$-DO, the diffraction peaks ascribed to the spinel structure

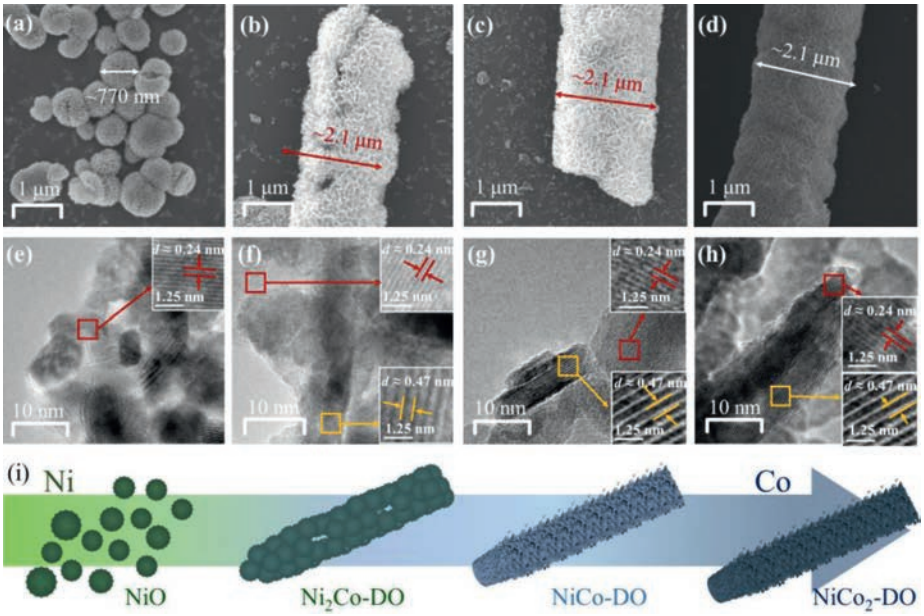

Fig. 1. SEM and HR-TEM images of (a, e) NiO, (b, f) Ni_2Co-DO, (c, g) NiCo-DO, and (d, h) $NiCo_2$-DO, respectively. (i) Schematic illustration of morphology variety of the above four samples.

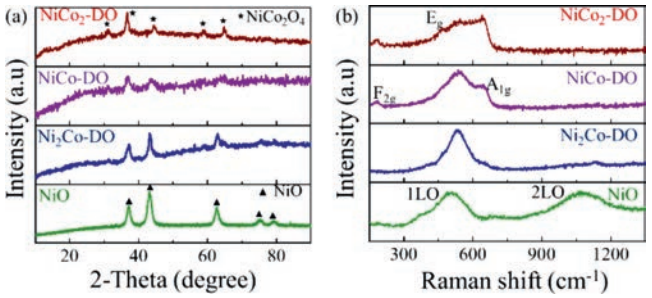

Fig. 2. (a) XRD patterns and (b) Raman spectra of NiO, Ni_2Co-DO, NiCo-DO, and $NiCo_2$-DO.

(JCPDS No. 20-0781) were observed due to the $NiCo_2O_4$ agglomeration. It was worth noting that the NiCo-DO sample exhibited the most weakened and broadened diffraction peaks in comparison with NiO, Ni_2Co-DO and $NiCo_2$-DO. It indicated that the incorporation of Co could largely distort the NiO lattice structure to low-crystalline and amorphous structure, but further facilitate the formation of $NiCo_2O_4$ nanocrystals.

To study the chemical structures of Ni_xCo_y-DO, Raman analysis was further performed. Fig. 2b showed that the one-phonon band (1LO, around 502 cm^{-1}) and two-phonon band (2LO, around 1065 cm^{-1}) in NiO were due to the Ni–O stretching mode. When incorporating Co^{2+} into NiO lattices, the 1LO band became more asymmetric and broader, and the 2LO peak decreased, which can be ascribed to the lattice expansion and structural disorder, along with oxygen vacancies [35]. In addition, the F_{2g}, E_g and A_{1g} bands at around 182, 466 and 642 cm^{-1}, respectively, were observed in both NiCo-DO and $NiCo_2$-DO, which can be attributed to the bridging metal-oxygen bonds (Ni-O and Co-O). The increased A_{1g} band in $NiCo_2$-DO demonstrated the increased concentration of octahedral coordination sites (CoO6, Co^{3+}) in the spinel $NiCo_2O_4$ structure [36], which was consistent with the XRD results.

Furthermore, the electronic structures of Ni and Co was studied by X-ray absorption near edge structure (XANES) spectroscopy. The normalized Co K-edge XANES spectra (Fig. S7a in Supporting information) showed that the Ni_2Co-DO was close to the CoO reference, but the NiCo-DO and $NiCo_2$-DO samples exhibited the similar pre-edge features with Co_3O_4, indicating that the Co valences in Ni_2Co-DO, NiCo-DO and $NiCo_2$-DO were dominantly Co(II), Co(II/III) and Co(II/III), respectively. On the other hand, all the as-prepared Ni_xCo_y-DO and NiO samples presented the similar structure of the standard NiO reference with Ni(II). While NiCo-DO and $NiCo_2$-DO exhibited relatively low white-line intensities, it revealed an increase of Ni(II) species with defects (Fig. S7b in Supporting information). The Fourier-transforms of the extended X-ray absorption fine structure (EXAFS) spectra of Co and Ni were collected to further analyze the Ni_xCo_y-DO samples. As shown in Fig. S7c (Supporting information), the peaks of Ni_2Co-DO were similar with standard CoO. However, NiCo-DO and $NiCo_2$-DO were close to Co_3O_4 with three characteristic peaks at 1.5, 2.5 and 3 Å, signified the bond distance of Co–O, octahedral Co-octahedral Co/Ni, and tetrahedral Co-octahedral Co, respectively. Meanwhile, the single scattering paths of Ni–O and the closest neighboring metal-metal (*i.e.*, octahedral Ni-octahedral Ni/Co) were observed at about 1.6 and 2.5 Å, respectively (Fig. S7d in Supporting information) [37]. Particularly, the intensity of Ni–O bonding was firstly reduced and then increased by increasing the Co content. The weakest intensity of Ni–O bonding in NiCo-DO indicated that the NiCo-DO possessed the minimal Ni–O bonding, which could be associated with the oxygen vacancies. Moreover, the bond distances of Ni–O and octahedral Ni-octahedral Ni/Co decreased with the increase of Co content, which was due to the difference of ion radius between Ni(II) and Co(II) [38].

The surface chemical structure was further measured by X-ray photoelectron spectroscopy (XPS). Fig. 3a showed the presence of Ni 2p, Co 2p and O 1s in the Ni_xCo_y-DO samples, All the chemical composition of as-prepared NiO and Ni_xCo_y-DO was listed in Table S3 (Supporting information). In addition, the Co 2p spectra (Fig. 3b) showed that Co(III) and Co(II) were found at 779.6 eV/794.9 eV and 781.2 eV/796.4 eV, respectively; meanwhile, the Ni 2p spectra (Fig. 3c) were also fitted with Ni(II) (854.3 eV/872.1 eV) and Ni(III) (855.6 eV/873.2 eV) [39]. With the increase of Co content, the Co(III)/Co(II) atomic ratio was increased as following: Ni_2Co-DO < NiCo-DO < $NiCo_2$-DO, and the trend of Ni(III)/Ni(II) atomic ratio was also increased (*i.e.*, NiO < Ni_2Co-DO < NiCo-DO < $NiCo_2$-DO, Table S3 in Supporting information). The high content of Co(III) and Ni(III) was designated to the partly per-oxidized surface and/or the formation of $NiCo_2O_4$ from NiO [26,40], both leading to an increase in surficial oxygen content (NiO < Ni_2Co-DO < $NiCo_2$-DO). However, it was worth noting that the NiCo-DO possessed the lowest oxygen content among the Ni_xCo_y-DO samples. The O 1s spectra (Fig. 3d) of the NiO and Ni_xCo_y-DO samples were deconvoluted into three fitted peaks centered at 529.2 eV (O1), 530.7 eV (O2) and 533.4 eV (O3), corresponding to the typical of lattice metal-oxygen bonds, the surficial oxygen deficient regions, and the multiplicity of hydroxyl physic/chemisorption, respectively [39]. The contents of the active O2 and O3 species were increased by introducing Co and increasing Co content (Table S3). Due to the largest structural distortion and the lowest oxygen content, the NiCo-DO exhibited the abundant surficial oxygen vacancies within the highly active surface. Thus, we estimated that the NiCo-DO would have the enhanced electrochemical sensing performance.

Before evaluating the performance for H_2O_2 detection, the NiO and all Ni_xCo_y-DO modified GCEs were activated by cyclic voltammetry (CV) measurement. Fig. 4a demonstrated the CV

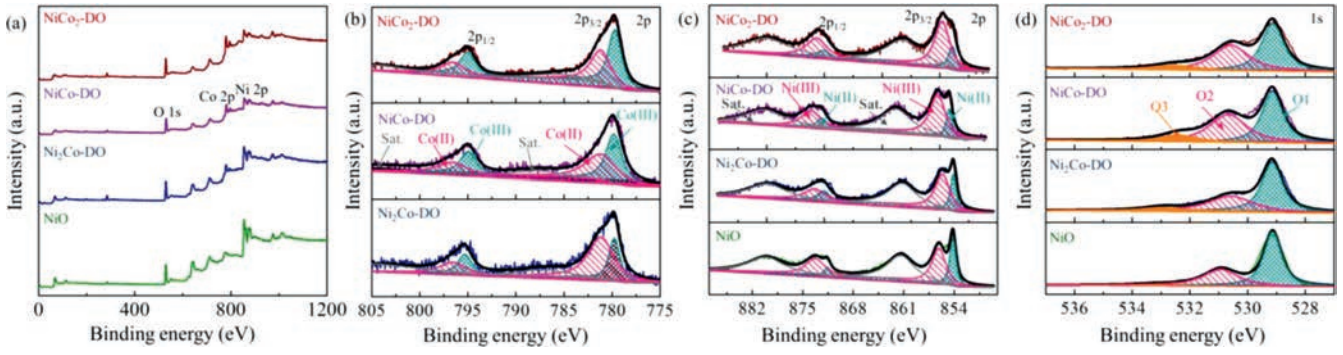

Fig. 3. XPS spectra of NiO and Ni_xCo_y-DO samples, (a) survey spectrum, (b) Co 2p, (c) Ni 2p, and (d) N 1s for the NiO and Ni_xCo_y-DO samples.

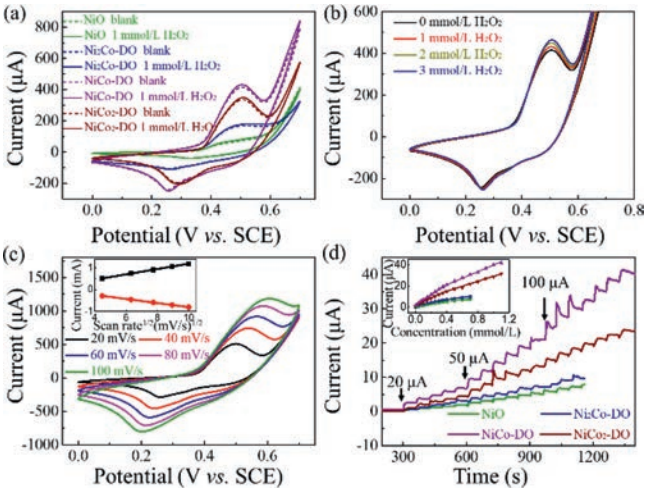

Fig. 4. (a) CV curves of the NiO and Ni_xCo_y-DO electrodes in absence and presence of 1 mmol/L H_2O_2. (b) CV curves of the NiCo-DO electrode in 0.1 mol/L NaOH with different content of H_2O_2. (c) CV curves of NiCo-DO at different scan rates, and the inset showed the derived plot of the redox peak *vs.* the square root of scan rate. (d) The *i-t* response of NiO and Ni_xCo_y-DO electrodes towards the injection of H_2O_2, and the inset in (d) showed the calibration curve of current response *vs.* H_2O_2 concentration.

curves of NiO and Ni_xCo_y-DO electrodes with and without 1 mmol/L H_2O_2 in 0.1 mol/L NaOH (N_2-saturated) solution at a scan rate of 20 mV/s. A pair of redox peaks within 0−0.70 V could be attributed to reversible processes between metal oxides and metal oxyhydroxides in the NaOH electrolyte. Compared with the NiO and Ni_2Co-DO (NiO: 46 μA; Ni_2Co-DO: 161 μA, at about 0.45 V), the NiCo-DO and $NiCo_2$-DO electrodes exhibited higher oxidation current (NiCo-DO: 415 μA; $NiCo_2$-DO: 337 μA) detection at about 0.50 V. Notably, the NiCo-DO exhibited the highest oxidation current responses (Δi = 16.7 μA) to 1 mmol/L H_2O_2 solution in comparison with other as-prepared electrodes ($NiCo_2$-DO: 12.7 μA; Ni_2Co-DO: 10.8 μA; NiO: 7 μA). Moreover, as the concentration of H_2O_2 increased, the cathodic current of the NiCo-DO sensor was significantly enhanced, indicating a typical representation of the catalytic reduction of H_2O_2 (Fig. 4b). The CV curves of NiCo-DO sensor under different scan rates (20 ~ 100 mV/s) were carried out to further study the electrochemical mechanism (Fig. 4c). The current responses exhibited a pair of redox peaks (the anodic peaks at *ca.* 0.49 ~ 0.60 V and the cathodic peaks at *ca.* 0.20 ~ 0.26 V). In addition, the redox peak currents maintained proportional to the square root of scan rate (the inset in Fig. 4c). The result indicated that the oxidation process of H_2O_2 on the NiCo-DO surface was diffusion controlled.

The amperometry curve of the NiO and NiCo-DO electrodes were carried upon the successive addition of H_2O_2 at +0.50 V (Fig. 4d). The corresponding calibration curves (the inset in Fig. 4d) showed that NiCo-DO exhibited a highest sensitivity of 698.605 μA L $mmol^{-1}$ cm^{-2}, with the linear range of 0 to 0.4 mmol/L and 444.84 μA L $mmol^{-1}$ cm^{-2}, with the linear range of 0.4–1.2 mmol/L towards the addition of H_2O_2, which was consistent with the CV results. Like other metal oxides, the decrease of sensitivity (slope) in the second linear range (higher analyte concentrations) [41,42], which was likely due to the limited specific surface area of Ni_xCo_y-DO restricted the diffusion of electrolyte and reactant [34]. In the future, we will further enlarge the range of linear region by loading Ni_xCo_y-DO on high surface area carriers. Besides, the NiCo-DO sensor also exhibited a low detection limit (0.28 μmol/L, S/N = 3). The calculation method of the sensitivity and the detection limit could be found in the

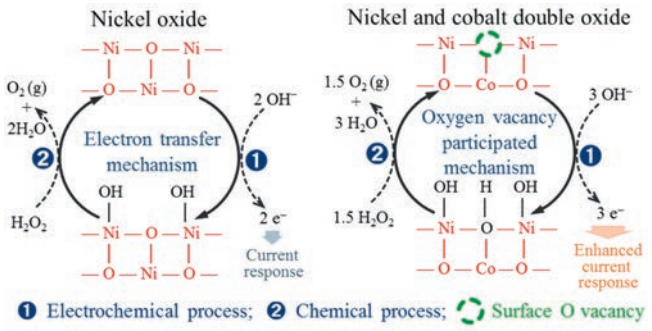

Scheme 1. Schematics of the electron transfer mechanism and the oxygen vacancy participated mechanism.

Supporting information. In addition, as aliquots of H_2O_2 were added into electrolyte, the response time of NiCo-DO was within 6 s. We also compared the sensing performances of NiCo-DO sensor with other typical non-enzymatic for H_2O_2 sensing. The summarized results showed that the detection performance of the NiCo-DO electrode was comparable even better than previous sensors, especially the sensitivity (Table S4 in Supporting information).

The excellent sensitivity and outstanding detection limit of NiCo-DO sample had drawn our attention. Based on the identification of the abundant surficial oxygen vacancies, we proposed the oxygen vacancy participated mechanism shown schematically in Scheme 1 in comparison with traditional electron transfer mechanism. Compared with the NiO, the oxygen-vacancy enriched NiCo-DO could enhance the surface activity and show the larger current response.

In addition, some potentially oxidizable compounds such as uric acid (UA), L(+)-cysteine (L-Cys) and ascorbic acid (AA) are the main interfering substances for H_2O_2 detection, for these electroactive species commonly coexisting in the biological fluids, which can also be oxidized at the high potential and their electrochemical signals to severely affect the selectivity of enzymatic sensors. Thus, it is critically important to examine the selectivity analysis of the NiCo-DO electrode towards H_2O_2 sensing. Fig. S8 (Supporting information) showed the chronoamperometric responses upon the addition of some possible interfering substances. 20 μmol/L additions of these interfering species exhibited negligible current responses, while 200 μmol/L H_2O_2 caused a significant response. It indicated that the NiCo-DO sensor had a good selectivity for H_2O_2 detection. Furthermore, the stability of the NiCo-DO electrode was studied by the five continuous chronoamperometry results in one month (stored at 4 °C, Fig. S9 in Supporting information). The attenuation of normalized current was only 14.2%, showing that the NiCo-DO sensor exhibited the excellent stability. The chronoamperometry measurement also showed a good reproducibility of NiCo-DO sensor with the relative standard deviation of only 5.80% in five parallel samples (Fig. S10 in Supporting information).

In summary, we synthesized a series of honeycomb-like open porous microarchitecture in built of the low-dimensional Ni_xCo_y-DO blocks with the different ratios of Ni/Co by a polyol-mediated solvothermal method. The introduced Co in Ni_xCo_y-DO not only induced the morphologic and crystalline change but also increased the surficial oxygen vacancies. Thanks to the abundant oxygen vacancies, the NiCo-DO sample presented the high sensitivity and low limit detection, along with the good selectivity, stability and reproducibility. Therefore, this work develops one kind of high-performance non-enzymatic H_2O_2 sensors and lends a new impetus to the potentially application of double metal oxides.

Declaration of competing interest

The authors declare that they have no known competing financial interests or personal relationships that could have appeared to influence the work reported in this paper.

Acknowledgments

This work was supported by the National Natural Science Foundation of China (Nos. 51432003, 51802011 and 51125007), the Start-Up Fund for Talent Introduction of Beijing University of Chemical Technology (No. buctrc201806), and the Fundamental Research Funds for the Central Universities (No. JD2010). The authors are grateful to the Beijing Synchrotron Radiation Facility (BSRF) for the XAFS tests.

Appendix A. Supplementary data

Supplementary material related to this article can be found, in the online version, at doi:https://doi.org/10.1016/j.cclet.2020.07.045.

References

[1] W. Liu, C.J. Lei, H.X. Zhang, et al., Chin. Chem. Lett. 28 (2017) 1306–1311.
[2] H.Y. Liu, H. Ma, H.H. Xu, et al., Anal. Bioanal. Chem. 411 (2019) 129–137.
[3] M. Zhang, Z.Z. Huang, G.Y. Zhou, et al., Anal. Method 7 (2015) 8439–8444.
[4] Y.G. Qin, Y.J. Sun, Y.J. Li, et al., Chin. Chem. Lett. 31 (2020) 774–778.
[5] K.L. Wu, B.C. Yang, X.X. Zhu, et al., New J. Chem. 42 (2018) 18749–18758.
[6] F. Vetr, Z. Moradi-Shoeili, S. Özkar, Appl. Organometal. Chem. 32 (2018) 1–10.
[7] A.S. Ivanova, A.D. Merkuleva, S.V. Andreev, K.A. Sakharov, Food Chem. 283 (2019) 431–436.
[8] R.C. Matos, E.O. Coelho, C.F. Souza, F.A. Guedes, M.A.C. Matos, Talanta 69 (2006) 1208–1214.
[9] J.W. Nai, S.Q. Wang, Y. Bai, L. Guo, Small 9 (2013) 3147–3152.
[10] X.B. Lu, G.F. Zou, J.H. Li, et al., J. Mater. Chem. 17 (2007) 1427–1432.
[11] T. Xiao, J.S. Huang, D.W. Wang, T. Meng, X. Yang, Talanta 206 (2020) 120210.
[12] Z.H. Wen, S.Q. Ci, J.H. Li, J. Phys. Chem. C 113 (2009) 13482–13487.
[13] W. Chen, S. Cai, Q.Q. Ren, W. Wen, Y.D. Zhao, Analyst 137 (2012) 49–58.
[14] S. Daemi, S. Ghasemi, A. Akbar Ashkarran, J. Colloid Interface Sci. 550 (2019) 180–189.
[15] A.M. Fekry, M. Shehata, S.M. Azab, A. Walcarius, Sens. Actuator B-Chem. 302 (2020) 1–11.
[16] Y. Shu, Y. Yan, J.Y. Chen, et al., ACS Appl. Mater. Interfaces 9 (2017) 22342–22349.
[17] P. Salazar, V. Rico, A.R. González−Elipe, Electrochim. Acta 235 (2017) 534–542.
[18] Z.Y. Yu, H.J. Li, X.M. Zhang, N.K. Liu, X. Zhang, Talanta 144 (2015) 1–5.
[19] W. Liu, H.X. Zhang, B. Yang, et al., Electroanal Chem. 749 (2015) 62–67.
[20] A.A. Ezhilarasi, J.J. Vijaya, K. Kaviyarasu, et al., J. Photochem. Photobiol. B 164 (2016) 352–360.
[21] S. Veeralingam, S. Priya, S. Badhulika, Chem. Eng. J. 389 (2020) 124415.
[22] H. Zhang, S. Liu, Sens. Actuator. B: Chem. 238 (2017) 788–794.
[23] L.Y. Yan, X.F. Wang, Q.T. Li, et al., Croat. Chem. Acta 89 (2016) 331–337.
[24] Y. Zhou, X. Ni, Z. Ren, et al., RSC Adv. 7 (2017) 45177–45184.
[25] X.Y. Zhao, J. Meng, Z.H. Yan, F.G. Cheng, J. Chen, Chin. Chem. Lett. 30 (2019) 319–323.
[26] T. Cai, J. Yuan, L. Zhang, et al., Catal. Sci. Technol. 8 (2018) 5416–5427.
[27] Y.X. Bao, P. Liu, J.X. Zhang, et al., J. Am. Ceram. Soc. (2020) 1–10.
[28] X.Y. Liu, Y.Q. Zhang, X.H. Xia, et al., J. Power Sources 239 (2013) 157–163.
[29] Y.N. Li, T. Wu, K.D. Jiang, et al., J. Mater. Chem. C 4 (2016) 7119–7129.
[30] B. Liu, S.H. Yu, L.J. Li, et al., Angew. Chem. Int. Ed. 43 (2004) 4745–4750.
[31] P. Zhou, Y.Y. Wang, C. Xie, et al., ChemComm. 53 (2017) 11778–11781.
[32] S.R. Chen, M. Xue, Y.Q. Li, et al., J. Mater. Chem. A 3 (2015) 20145–20152.
[33] C.X. Huang, Y.H. Ding, C. Hao, et al., Chem. Eng. J. 378 (2019) 122202.
[34] Q. Li, W.B. Gao, X.P. Zhang, et al., RSC Adv. 8 (2018) 13401–13407.
[35] A. Alshahrie, Superlattice. Microst. 96 (2016) 75–81.
[36] Z.J. Liu, Z.H. Xiao, G. Luo, et al., Small 15 (2019) 1904903.
[37] J.W. Nai, H.J. Yin, T.T. You, et al., Adv. Energy Mater. 5 (2015) 1401880.
[38] T.H. Lim, S.J. Cho, H.S. Yang, M.H. Engelhard, D.H. Kim, Appl. Catal. A-Gen. 505 (2015) 62–69.
[39] D.D. Wang, Z.X. Cuo, S.D. Li, M. Zhang, Y.F. Chen, CrystEngComm 22 (2020) 2371–2379.
[40] Z.P. Zhang, Y.S. Qin, M.L. Dou, Nano Energy 30 (2016) 426–433.
[41] N.H. Al-Hardan, M.A. Abdul Hamid, R. Shamsudin, N.K. Othman, L.K. Keng, Sensors 16 (2016) 1–8.
[42] D.Z. Chen, D. Pang, S.P. Zhang, et al., Electrochim. Acta 330 (2020) 1–11.